



Topological Invariants for Low-Energy Massive Dirac Systems

Iqra Fraz¹ and Kulsoom Rahim¹

Department of Basic Sciences, University of Engineering and Technology, Taxila

ABSTRACT

We study the photon-dressed electronic band structure of topological insulator thin films doped by magnetic impurities under an off-resonance time-periodic electromagnetic field. The thin films irradiated by circularly polarized light undergo phase transitions, leading to distinct phases depending on the frequency, intensity, and polarization of the light. Topological materials have gained importance due to their potential applications in spintronics and quantum computing. This research examines how circularly polarized light influences the electronic properties of the topological insulator BiSb_2Te_3 , incorporating the quadratic momentum term $\frac{\hbar^2 k^2}{2m}$ into the Hamiltonian. The research demonstrates that specific topological phases form when light-induced modifications lead to a Quantum Pseudo-Spin Hall Insulator (QPHI) and a Quantum Anomalous Hall Insulator (QAHI). Our findings reveal the complete phase diagrams, illustrating how external electromagnetic fields facilitate topological transition tuning. This study enhances the understanding of how to engineer Dirac material phases using light while establishing theoretical foundations for experimental investigations in quantum transport and optoelectronics.

1. Introduction

Scientists have intensively searched for Dirac-like materials since topological insulators were discovered in order to discover electronic structures that conform to Dirac equations like graphene and Bi_2Se_3 [1, 2]. During many years, researchers discovered that $(\text{Bi}, \text{Sb})_2\text{Te}_3$ family compounds display topological phases when exposed to external perturbations and that Cr-doped $(\text{Bi}, \text{Sb})_2\text{Te}_3$ serves as the central component for observing the quantum anomalous Hall effect (QAHE) [3, 4]

A successful method exists for controlling topological systems at the band structure level using light-matter coupling phenomena. Scientists have proven that exposing Dirac materials to circularly polarized light leads to the creation of photo-induced topological phases according to research in [5]. Time-reversal symmetry breaking in combination with irradiation creates a gap around the Dirac point to form a Floquet topological insulator [6]. Researchers have achieved Floquet engineering in solid-state systems which enables them to fabricate distinctive quantum state platforms [7]

This work investigates a topological system derived from BiSb_2Te_3 material through the addition of a quadratic momentum term to the Hamiltonian to obtain improved electronic structure precision and maintain topological characteristics as reported in [8]. Our investigation stems from theoretical studies that analyzed band gap transformations from light exposure and their consequences on Berry curvature alongside Chern number [9]. The study uses these analytical parameters to identify how external light fields affect topological phase transitions.

In many 2D and 3D systems, the quadratic momentum contribution to dispersion is also considerable. A quadratic in momentum term in Weyl semimetals breaks inversion and time-reversal symmetry. A quadratic momentum term in Weyl semimetals breaks inversion and time-reversal symmetry [11, 10]. In the absorption component of Hall conductivity, the asymmetry results in an oscillation pattern and two-peak structure [?]. In the linear background of optical conductivity of the Weyl semimetal, the asymmetry results in an oscillation pattern with two peak structure [12]. The absorption lines have a two-peak shape that is typical of the Schrödinger component of the Hamiltonian. [13]

2. Effective Low-Energy Hamiltonian

2.1 Dark Hamiltonian

In an ultra-thin film of TI materials such as the $(\text{Bi}, \text{Sb})_2\text{Te}_3$ family, two Dirac cones, associated with the helical surface states on the top and bottom surfaces, are hybridized with each other. As a result, tunneling between the two surface states opens a gap in the band structure. On the other hand, a strong perpendicular ferromagnetism emerges in this thin film arising from the interaction between doped magnetic impurities. The resultant magnetization is assumed as a new control parameter of the gap size, and the new quantum phase is QAHI.

The effective low-energy Hamiltonian for the hybridized Dirac cones near the Γ point is given by [14]

$$H_{\text{dark}}(k) = \frac{\hbar^2 k^2}{2m} \sigma_0 + \hbar v_f (k_y \sigma_x - k_x \sigma_y) \otimes \tau_z + \Delta(k) \sigma_0 \otimes \tau_x + V_{\text{sia}} \sigma_0 \otimes \tau_z + M_z \sigma_z \otimes \tau_0. \quad (1)$$

Here, σ_0 and τ_0 are 2×2 identity matrices, while τ_i and σ_i ($i = x, y, z$) are the Pauli matrices represented in the basis sets of the thin film upper and lower surfaces states $\{|u\rangle, |l\rangle\}$ and the electron spin states $\{|\uparrow\rangle, |\downarrow\rangle\}$, respectively.

The mass term Δ induced by tunneling between the top and bottom surfaces is experimentally mapped to:

$$\Delta(k) = \Delta_0 + \Delta_1 k^2, \quad (2)$$

for films of Bi_2Se_3 and the $(\text{Bi,Sb})_2\text{Te}_3$ family thinner than 10 nm [15, 16]. In this work, in our numerical calculations, we consider system parameters as $\Delta_0 = 35$ meV and $\Delta_1 = 10$ eV $\cdot\text{\AA}^{-2}$ at the Fermi velocity $v_f = 4.48 \times 10^5$ m/s.

To guarantee the off-resonant regime, the external Floquet field has $\hbar\Omega$ far away or replicas, since the driven frequency has $\hbar\Omega = 1$ eV, which is higher than the band width.

The SIA potential, V_{sia} , appearing in the third term is caused by a kind of perpendicular potential difference induced by the applied electric field or also by the substrate [15], giving rise to a Rashba-like splitting of the band spectrum. Indeed, the SIA potential depends on the two surface Dirac cones upward and downward, and may stem from the finite thickness of the film, which on the substrate is weaker in thinner films.

Thus, this term originates from the difference between the environment of the top and bottom surfaces, which is stronger for thinner films [15]. The last term in Eq. (1) refers to the perpendicular strong ferromagnetic exchange field which originates from the magnetic impurities such as Ti, V, Cr, and Fe in Bi_2Se_3 and $(\text{Bi,Sb})_2\text{Te}_3$ family [17].

Equation (1) expresses the Hamiltonian in the spin-surface basis spanned by the basis set $\{|\uparrow, u\rangle, |\downarrow, u\rangle, |\uparrow, l\rangle, |\downarrow, l\rangle\}$. In some occasions, it is more convenient to use a representation connected to the surface states and work in the bonding and anti-bonding states $|\psi_{b,a}\rangle = (|u\rangle \pm |d\rangle)/\sqrt{2}$.

In terms of this basis $\{|\uparrow, b\rangle, |\downarrow, b\rangle, |\uparrow, a\rangle, |\downarrow, a\rangle\}$, the Hamiltonian is expressed as:

$$h_{\text{dark}}(k)_{\alpha_z} = \frac{\hbar^2 k^2}{2m} \sigma_0 + \hbar v_f (k_y \sigma_x - \alpha_z k_x \sigma_y) + (\Delta(k) + \alpha_z M_z) \sigma_z. \quad (3)$$

each of which has its own pseudo-spin band spectrum:

$$E_{\alpha_z}(k) = \frac{\hbar^2 k^2}{2m} \pm \sqrt{(\hbar v_f k)^2 + (\Delta_0 + \Delta_1 k^2 + \alpha_z M_z)^2} \quad (4)$$

2.2 Photo-Induced Hamiltonian

Let us now consider a high-frequency electromagnetic field with circular polarization irradiated on a thin film TI sample of magnetically doped Bi_2Se_3 or $(\text{Bi,Sb})_2\text{Te}_3$ family. The vector potential representing the magnetic component of the radiation is given by

$$\mathbf{A}(t) = A_0 (\sin \Omega t, \cos \Omega t) \quad (5)$$

where $\Omega = \frac{2\pi}{T}$ is the frequency of light so that $\mathbf{A}(t+T) = \mathbf{A}(t)$ while A_0 is adjustable in experiment by simply tuning the light intensity. Here, $\Omega > 0$ is attributed to the right-hand circularly polarized light while $\Omega < 0$ refers to a left-handed circular polarization. Radiation can be introduced into the Hamiltonian by replacing the wave-vector \mathbf{k} by $\mathbf{k} + \frac{e\mathbf{A}}{\hbar}$,

$$H(t) = H_{\text{dark}}\left(\mathbf{k} + \frac{e\mathbf{A}}{\hbar}\right). \quad (6)$$

We work in the off-resonant regime where Ω is much larger than the bandwidth of the system. Indeed, the bandwidth of the surface band structure is, at most, equal to the band gap of bulk Bi_2Se_3 or $(\text{Bi,Sb})_2\text{Te}_3$ family, i.e., ~ 0.3 eV. Therefore, taking 1 eV for the laser beam energy guarantees that the replicas of the bulk Floquet bands split up and, by varying the system parameters, there is no band touching of other Floquet side bands with the bulk Floquet band at zero energy.

Let us stress that in this work, we are focusing on the edge modes falling inside the band gap of the first bulk Floquet band, not on the edge modes appearing in the dynamical gaps. Moreover, the irradiated photon does not excite an electron directly but its effect is described by a time-averaged Hamiltonian.

For a very weak laser field of scaled strength $A \equiv \frac{eA_0}{\hbar} \ll \frac{1}{a_0}$, where $a_0 \approx 4 \text{\AA}$ is the lattice parameter of $(\text{Bi,Sb})_2\text{Te}_3$ family materials [18], the effective Hamiltonian for the high-frequency regime is expanded as [19, 20, 21]

$$H = H^0 + \sum_{j \neq 1}^{\infty} \frac{[H^{-j}, H^{+j}]}{j \hbar \Omega} + O\left(\frac{1}{(\hbar \Omega)^2}\right) \quad (7)$$

The Floquet Hamiltonian is given by:

$$H_n = \frac{1}{T} \int_0^T H(t) e^{in|\Omega|t} dt, \quad (8)$$

where $n = 0, \pm 1, \pm 2, \dots$ corresponds to the virtual absorption/emission of n photons.

$$h^0 = h_{\alpha_z}^{\text{dark}} + A^2 \alpha \sigma_0 + \Delta_1 A^2 \sigma_z. \quad (9)$$

and the one-photon assisted version of Eq. (3) reads:

$$h_{\pm \alpha_z} = \frac{\hbar^2 k^2}{2m} \sigma_0 + \frac{1}{2} \hbar v_f A (\sigma_x \mp i \alpha_z \sigma_y) + \Delta_1 A (\pm i k_x + k_y) \sigma_z. \quad (10)$$

The higher photon-assisted versions are equal to zero. The commutation between the two decoupled pseudo-spin Hamiltonians, namely

$$\frac{1}{\hbar \Omega} [h_{-\alpha_z}^{(1)}, h_{\alpha_z}^{(1)}] = \frac{2v_f}{\Omega} A^2 \Delta_1 (k_x \sigma_y - \alpha_z k_y \sigma_x) + \alpha_z m_\Omega \sigma_z, \quad (11)$$

leads to the effective static Hamiltonian

$$H_{\text{driven}}^{\alpha_z} = \frac{\hbar^2 k^2}{2m} \sigma_0 + \hbar \eta_{\alpha_z} v_f (k_y \sigma_x - \alpha_z k_x \sigma_y) + [\Delta'(k) + \alpha_z (M_z + m_\Omega)] \sigma_z. \quad (12)$$

with the definition

$$\Delta'(k) = \Delta_0 + \Delta_1 k^2, \quad \text{where } \Delta_0 = \Delta_0 + \Delta_1 A^2. \quad (13)$$

The band spectrum would be

$$E_{\alpha_z}(k) = \frac{\hbar^2 k^2}{2m} \sigma_0 \pm \sqrt{(\eta_{\alpha_z} \hbar v_f k)^2 + (\delta_{\alpha_z} + \Delta_1 k^2)^2} \quad (14)$$

for each of the pseudo-spin indices α_z . The mass term

$$m_\Omega = \frac{(\hbar v_f A)^2}{\hbar \Omega} \quad (15)$$

induced by light irradiation is grouped with the one in Eq. (3) into the modified total mass term

$$\delta_{\alpha_z} = \Delta_0 + \alpha_z (M_z + m_\Omega). \quad (16)$$

Interestingly, compared to the dark case described by Eqs. (3) and (4), v_f is now scaled by a factor

$$\eta_{\alpha_z} = 1 - \frac{2\alpha_z A^2 \Delta_1}{\hbar \Omega}. \quad (17)$$

This implies that the Fermi velocity of helical surface states is modulated depending on the light parameters. This is a hallmark of new topological phases in the irradiated material.

3 Topological Invariants

3.1 Topological Invariant for Dark Hamiltonian

For a Unperturbed Hamiltonian. The Total Chern Number is defined as

$$C = C_+ + C_- \quad (18)$$

and the total Chern number as

$$C = \frac{\alpha_z}{2} \text{sgn}(\Delta_1 - \delta_0) \quad (19)$$

By integrating the Berry Curvature

$$\Omega_{\alpha_z}(k) = -\frac{\alpha_z}{4\pi} \frac{\hbar^2 v_f^2 (\Delta_0 + \alpha_z M_z - \Delta_1 k^2)}{(\hbar^2 v_f^2 k^2 + (\Delta_0 + \alpha_z \Delta_1 k^2 + \alpha_z M_z)^2)^{3/2}} \quad (20)$$

3.2 Topological Invariant for Photo Induced Hamiltonian

For a Hamiltonian that commutes with the pseudo-spin operator $\hat{\alpha}_z$ and is thus block diagonal in the pseudo-spin space, the band spectrum splits into two \pm pseudo-spin bands with pseudo-spin Chern number C_{α_z} per each block [22, 23, 24, 25]. One defines the total Chern number as

$$C = C_+ + C_- \quad (21)$$

and the total pseudo-spin Chern number as

$$C_0 = \frac{\alpha_z}{2} (C_+ - C_-). \quad (22)$$

By integrating the Berry curvature

$$\Omega_{\alpha_z}(k) = -\frac{\alpha_z}{4\pi} \times 2\pi \frac{\hbar^2 v_f^2 \eta_{\alpha_z}^2 (\delta_{\alpha_z} - \Delta_1 k^2)}{(\hbar^2 v_f^2 \eta_{\alpha_z}^2 k^2 + (\delta_{\alpha_z} + \Delta_1 k^2)^2)^{3/2}}. \quad (23)$$

Over the whole Brillouin zone, one gains the Chern number for each pseudo-spin sector

$$C_{\alpha_z} = \frac{\alpha_z}{2} \text{sgn}(\Delta_1 - \delta_{\alpha_z}) \quad (24)$$

explicitly for TI thin films when there is no pseudo-spin conservation [24]. Since we set $V_{\text{sia}} = 0$, pseudo-spin is conserved in this work. It is interesting that the latter does not depend on η_{α_z} . Although Eq. (21) only works if the pseudo-spin is conserved, the pseudo-spin Chern number can still be defined in a tricky and complicated way even if α_z is not conserved [22, 23]. This definition is generally based on the smooth decomposition of the occupied valence band into two sectors during the diagonalization of the pseudo-spin operator $\hat{\alpha}_z$ in the valence band. This quantity has been calculated explicitly in Ref. [24] for TI thin films when there is no pseudo-spin conservation. Since we set V_{sia} to be zero, pseudo-spin is conserved in this work.

If time reversal symmetry is present (corresponding to $M_z = m_\Omega = 0$ in our model), $C_0 \bmod 2$ and the \mathbb{Z}_2 index [26] yield the same result, and both are topological invariants of the system. Such a relationship is thoroughly investigated for TI thin films in Ref. [24]. However, even if there is no time reversal symmetry so that the \mathbb{Z}_2 invariant is not well-defined, one can still use C_{α_z} . Nevertheless, C_{α_z} cannot protect the edge modes when both time reversal symmetry and pseudo-spin conservation are broken.

4 Result and Discussion

4.1 Energy Dispersion Analysis of Dark and Photo-Induced Hamiltonians

4.3.1 Energy Spectrum of the Dark Hamiltonian

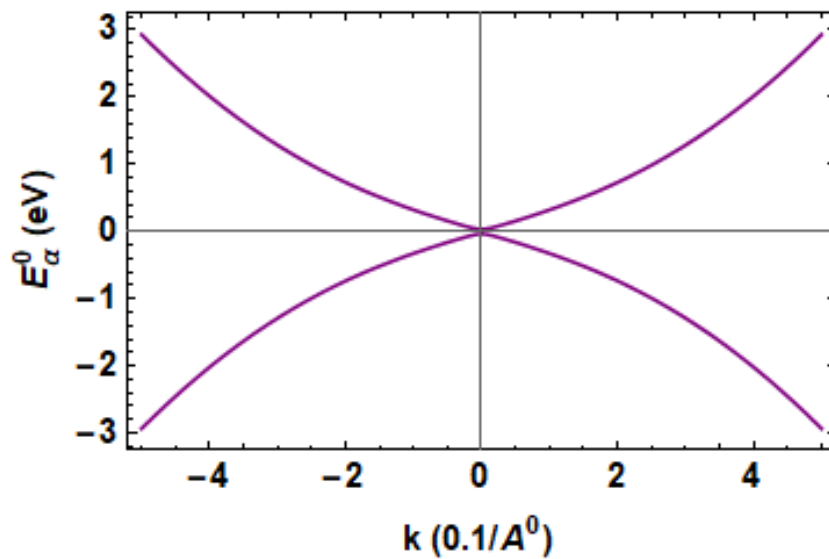


Figure 1(a): 2D plot of $E_{\alpha_z}^{(0)}(k)$ vs k Energy spectrum of the dark Hamiltonian showing symmetric positive and negative branches.

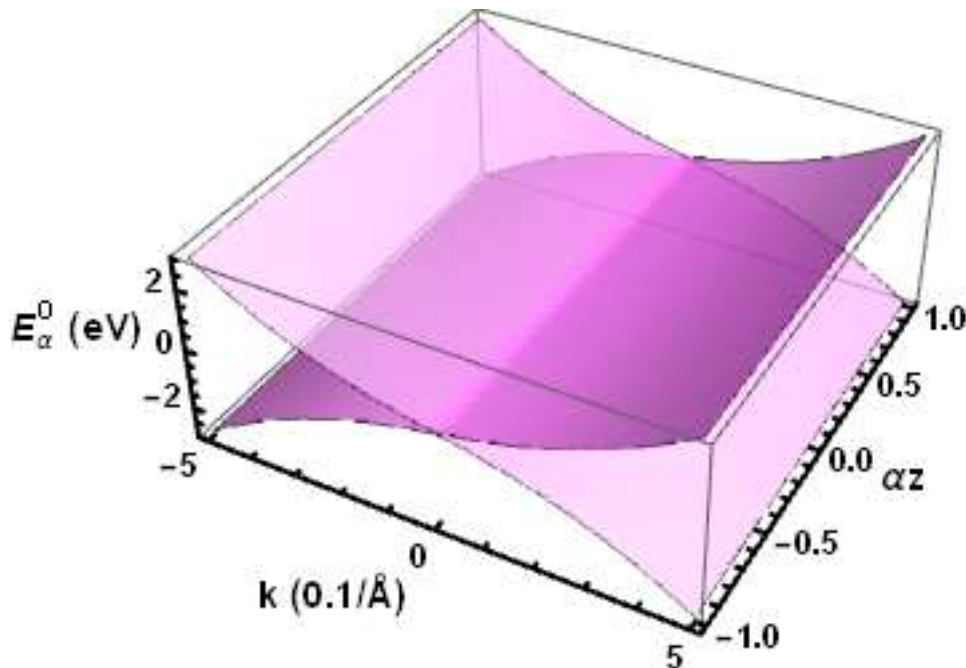


Figure 2(b): 3D plot of $E_{\alpha_z}^{(0)}(k)$ vs k Energy spectrum of the dark Hamiltonian showing symmetric positive and negative branches.

To Visualize the energy dispersion for the dark Hamiltonian, we numerically evaluate the energy eigenvalues as a function of crystal momentum k , using the relation:

$$E_{\alpha_z}^{(0)}(k) = \sqrt{(\hbar v_f k)^2 + (\Delta_0 + \Delta_1 k^2)^2}$$

Here, $\hbar = 6.5821 \times 10^{-16}$ eV · s is the reduced Planck constant, $v_f = 4.485 \times 10^5$ m/s is the Fermi velocity, $\Delta_0 = 0.035$ eV, and $\Delta_1 = 1 \times 10^{-19}$ eV · Å². We set $M_z = 0$ to isolate the intrinsic topological mass term in the absence of any external magnetic field or light-induced perturbation.

Using Mathematica, the positive and negative energy branches $\pm E_{\alpha_z}^{(0)}(k)$ were plotted over the range $k \in [-5, 5]$ Å⁻¹. The plot shows the characteristic Dirac-type dispersion, with the energy gap at $k = 0$ determined by $2\Delta_0$, confirming the gapped nature of the system in the absence of light. The results are visualized both in two and three dimensions.

In the 2D plot, the symmetric branches of the energy spectrum are plotted in purple, with clear labeling of the momentum axis and energy axis. Additionally, a 3D plot was generated over $\alpha_z \in [-1, 1]$, illustrating the symmetry of the energy spectrum with respect to the spin index α_z . The plots utilize dark axes, styled ticks, and neutral lighting for clarity and presentation suitability.

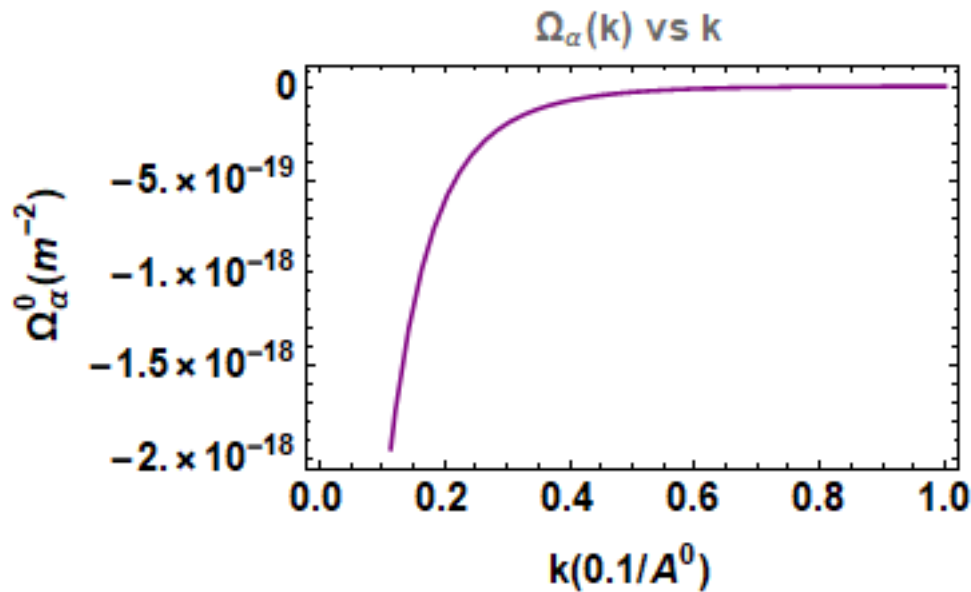


Figure 2(a): Berry curvature 2D plot of $\Omega_{\alpha_z}(k)$ vs. k

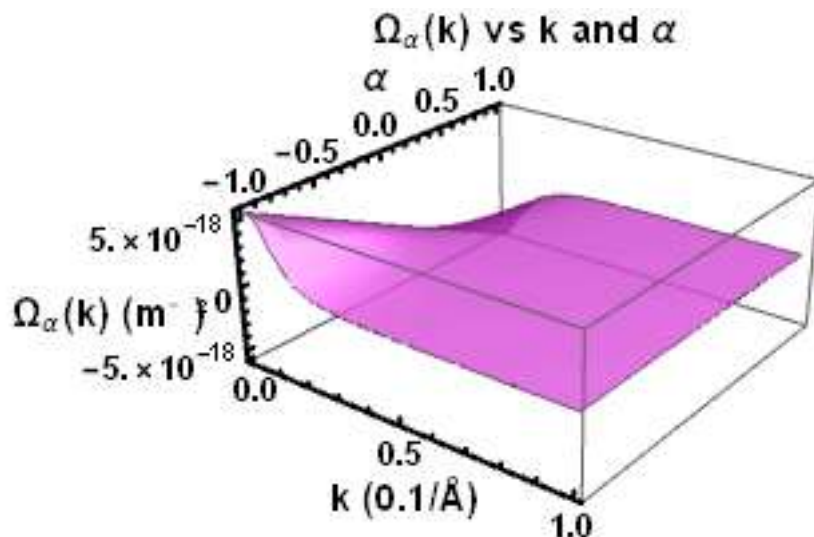


Figure 2(b): Berry curvature 3D plot of $\Omega_{\alpha_z}(k)$ vs. k

The Berry curvature $\Omega_{\alpha_z}(k)$ is computed for the light-induced Hamiltonian incorporating the modified parameters due to circularly polarized light. The velocity term is renormalized through η_{α_z} , which depends on the light amplitude A_0 , photon energy $\hbar\Omega$, and band index α_z .

The 2D plot in Fig. 2(a) shows the Berry curvature profile for $\alpha_z = 1$, where the curvature peaks around low values of k and decreases with increasing k . The 3D plot in Fig. 2(b) illustrates how the curvature evolves with both k and α_z , revealing the symmetry and topological behavior of the system under light exposure. The parameters used in this calculation are:

- $\hbar = 6.5821 \times 10^{-16} \text{ eV} \cdot \text{s}$
- $v_f = 4.485 \times 10^5 \text{ m/s}$
- $\Delta_0 = 35 \text{ meV}, \Delta_1 = 1 \times 10^{-19} \text{ eV} \cdot \text{\AA}^2$
- $M_z = 0, \hbar\Omega = 1 \text{ eV}$
- $A_0 = \frac{1}{3 \times 10^{-10}} \text{ m}^{-1}$

The effective mass term m_Ω and renormalized gap Δ_{α_z} were used to compute the curvature numerically.

The effective mass term m_Ω and renormalized gap Δ_{α_z} were used to compute the curvature numerically.

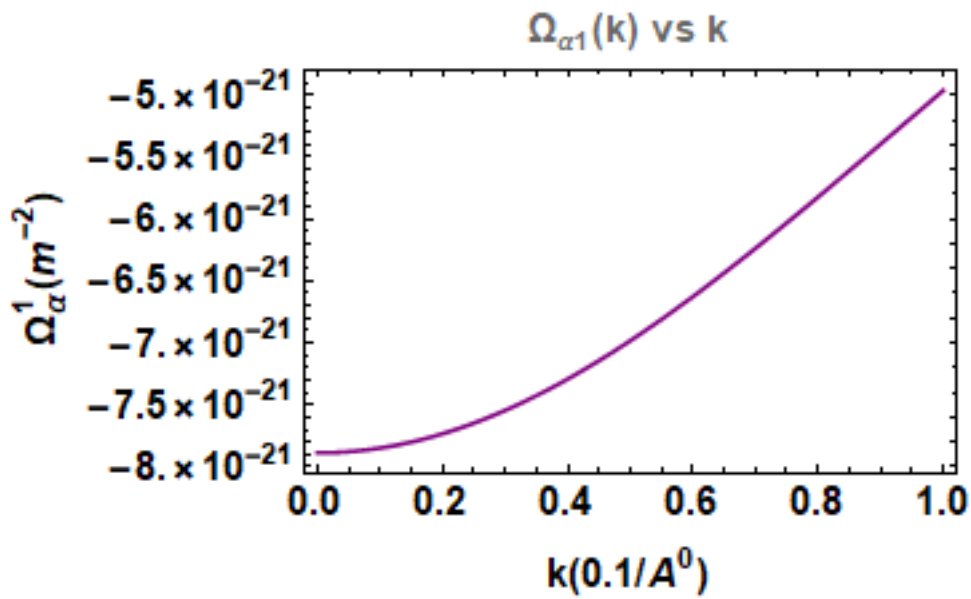


Figure 3(a): Berry curvature $\Omega_{\alpha_z}(k)$ for the light-induced Hamiltonian 2D plot of $\Omega_{\alpha_z}(k)$ vs. k for $\alpha_z=1$

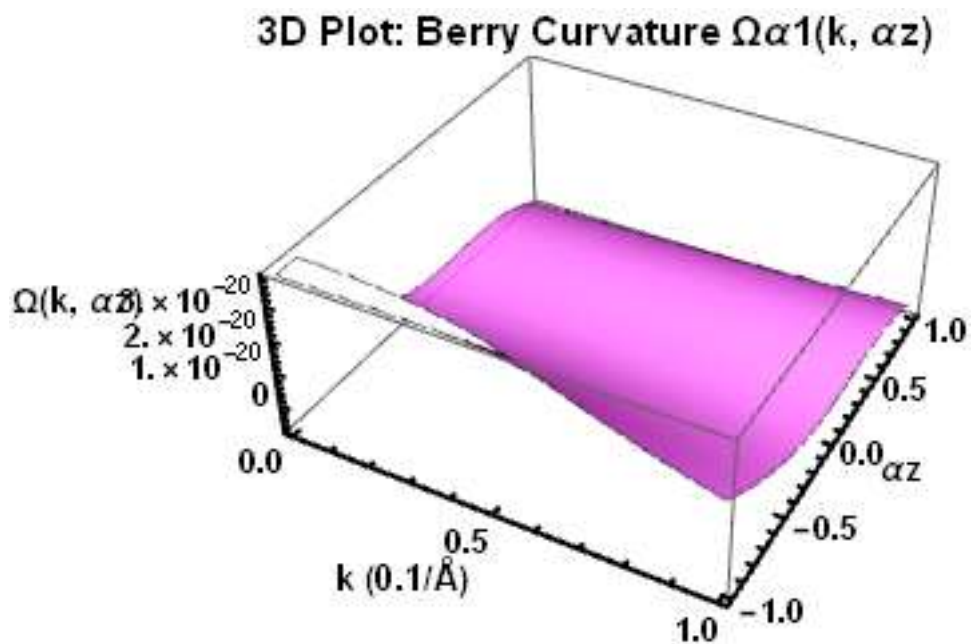


Figure 3(b): 3D plot of $\Omega_{\alpha_z}(k, \alpha_z)$ showing variation of Berry curvature with both momentum k and band index α_z .

The Berry curvature $\Omega_{\alpha_z}(k)$ is computed for the light-induced Hamiltonian incorporating the modified parameters due to circularly polarized light. The velocity term is renormalized through η_{α_z} , which depends on the light amplitude A_0 , photon energy $\hbar\Omega$, and band index α_z .

The 2D plot in Fig. 3(a) shows the Berry curvature profile for $\alpha_z = 1$, where the curvature peaks around low values of k and decreases with increasing k . The 3D plot in Fig. 3(b) illustrates how the curvature evolves with both k and α_z , revealing the symmetry and topological behavior of the system under light exposure.

The parameters used in this calculation are:

- $\hbar = 6.5821 \times 10^{-16} \text{ eV} \cdot \text{s}$
- $v_f = 4.485 \times 10^5 \text{ m/s}$
- $\Delta_0 = 35 \text{ meV}, \Delta_1 = 1 \times 10^{-19} \text{ eV} \cdot \text{\AA}^2$
- $M_z = 0, \hbar\Omega = 1 \text{ eV}$
- $A_0 = \frac{1}{3 \times 10^{-10}} \text{ m}^{-1}$

The effective mass term m_Ω and renormalized gap Δ_{α_z} were used to compute the curvature numerically.

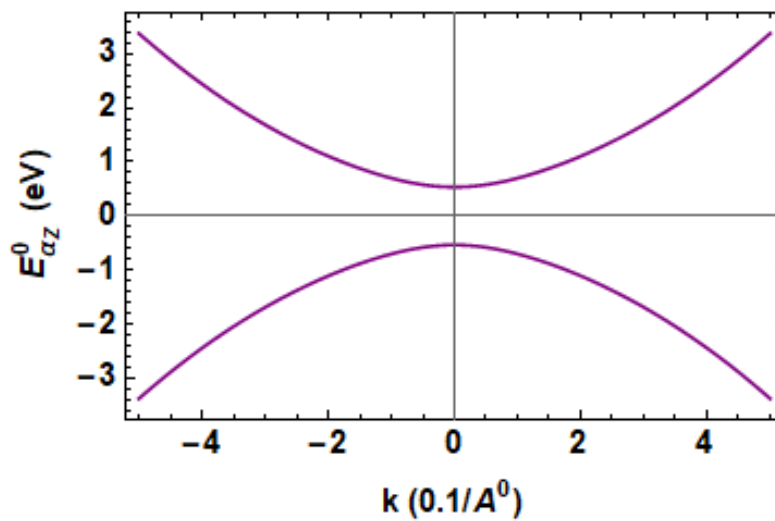


Figure 4(a): Energy spectrum $\pm E_{\alpha_z}^0(k)$ for the dark Hamiltonian. 2D plot showing symmetric conduction and valence bands for $\alpha_z = 1$.

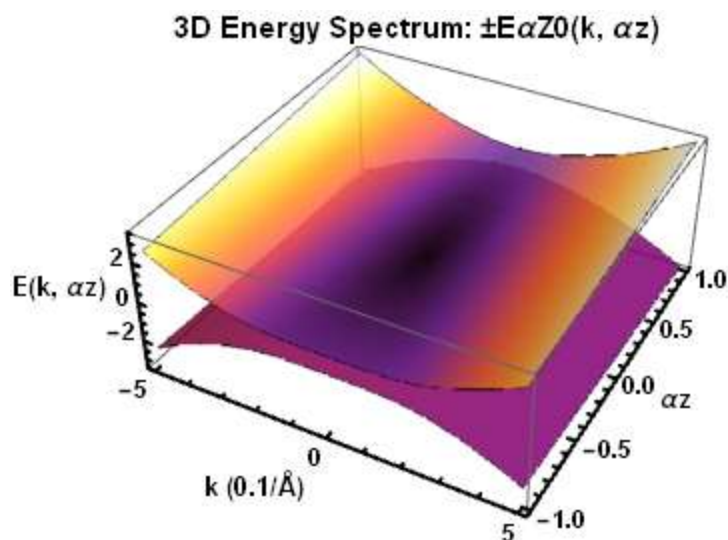


Figure 4(b): Energy spectrum $\pm E_{\alpha_z}^0(k)$ for the dark Hamiltonian. 3D energy band structure varying with both momentum k and band index α_z , with magnetic field $M_z = 0.5 \text{ eV}$

The energy dispersion relation for the dark Hamiltonian is given by:

$$E_{\alpha_z}^0(k) = \sqrt{(\hbar v_f k)^2 + (\Delta_0 + \Delta_1 k^2 + \alpha_z M_z)^2}$$

where v_f is the Fermi velocity, Δ_0 and Δ_1 define the mass term, and M_z is the magnetization-induced exchange field.

Fig. 4(a) shows the symmetric energy bands $\pm E_{\alpha_z}^0(k)$ for $\alpha_z = 1$, highlighting the presence of a finite energy gap due to magnetic doping. The 3D plot in Fig. 4(b) further illustrates how the energy bands vary with the momentum k and band index α_z , confirming the gap opening due to $M_z = 0.5$ eV.

The parameters used are:

- $\hbar = 6.5821 \times 10^{-16}$ eV · s
- $v_f = 4.485 \times 10^5$ m/s
- $\Delta_0 = 35$ meV, $\Delta_1 = 1 \times 10^{-19}$ eV · Å²
- $M_z = 0.5$ eV

These results are consistent with the expected behavior of magnetically doped topological insulators in the off-resonant regime.

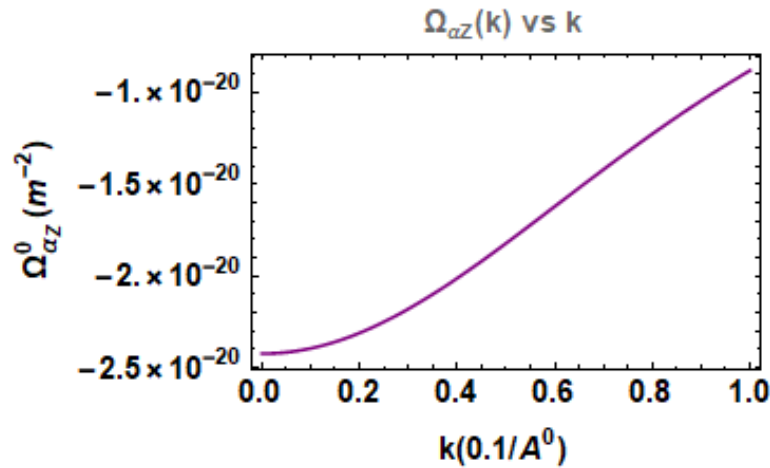


Figure 5(a): Berry curvature $\Omega_{\alpha_z}^0(k)$ for the dark Hamiltonian. Left: 2D plot of Berry curvature vs k for $\alpha_z = 1$, showing strong peak around $k = 0$.

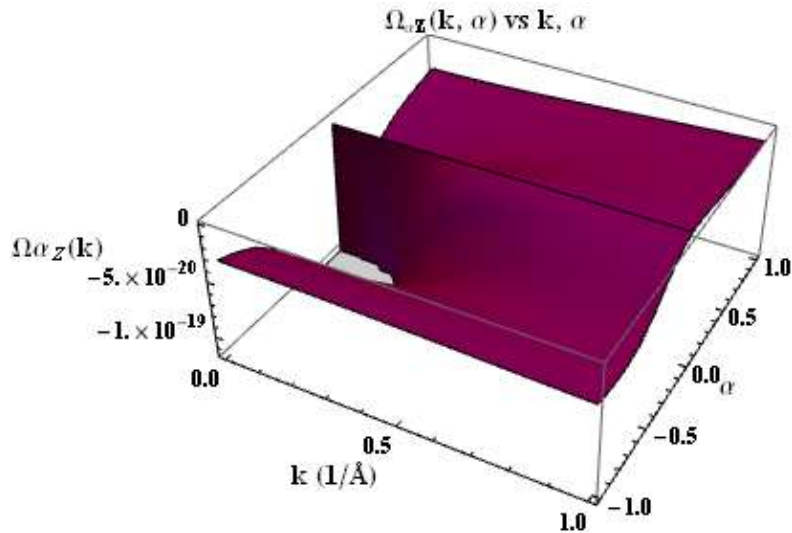


Figure 5(b): Berry curvature $\Omega_{\alpha_z}^0(k)$ for the dark Hamiltonian. 3D surface showing dependence of $\Omega_{\alpha_z}^0(k, \alpha_z)$ on both momentum k and band index α_z , with $M_z = 0.5$ eV.

The Berry curvature $\Omega_{\alpha_z}^0(k)$ is calculated for the dark Hamiltonian using the expression:

$$\Omega_{\alpha_z}^0(k) = -\frac{\alpha_z}{4\pi} \frac{\hbar^2 v_f^2 (\Delta_0 + \alpha_z M_z - \Delta_1 k^2)}{(\hbar^2 v_f^2 k^2 + (\Delta_0 + \Delta_1 k^2 + \alpha_z M_z)^2)^{3/2}}$$

Figure 5(a) shows the 2D Berry curvature profile, which peaks around $k = 0$ and decays with increasing k . The curvature's sign and magnitude depend on α_z , indicating different topological behavior for upper and lower bands. The 3D plot in Fig. 5(b) displays the variation of $\Omega_{\alpha_z}^0$ with both k and α_z , helping visualize the contribution to the Chern number from each band.

The following parameters were used:

- $\hbar = 6.5821 \times 10^{-16} \text{ eV} \cdot \text{s}$
- $v_f = 4.485 \times 10^5 \text{ m/s}$
- $\Delta_0 = 35 \text{ meV}, \Delta_1 = 1 \times 10^{-19} \text{ eV} \cdot \text{\AA}^2$
- $M_z = 0.5 \text{ eV}$

The sign of the Berry curvature determines the sign of the Chern number, and thus the topological nature of the system.

Photo-Induced Driven Hamiltonian

Under off-resonant circularly polarized light, the static Hamiltonian is modified via the Floquet formalism. The resulting photo-induced (driven) Hamiltonian affects both the kinetic and mass terms. and the constants used are:

- $\hbar = 6.5821 \times 10^{-16} \text{ eV} \cdot \text{s}$
- $v_f = 4.485 \times 10^5 \text{ m/s}$
- $\Delta_0 = 35 \text{ meV}, \Delta_1 = 1 \times 10^{-19} \text{ eV} \cdot \text{\AA}^2$
- $M_z = 0.5 \text{ eV}, \hbar\Omega = 1 \text{ eV}$
- $A_0 = \frac{1}{3 \times 10^{-10}} \text{ m}^{-1}$

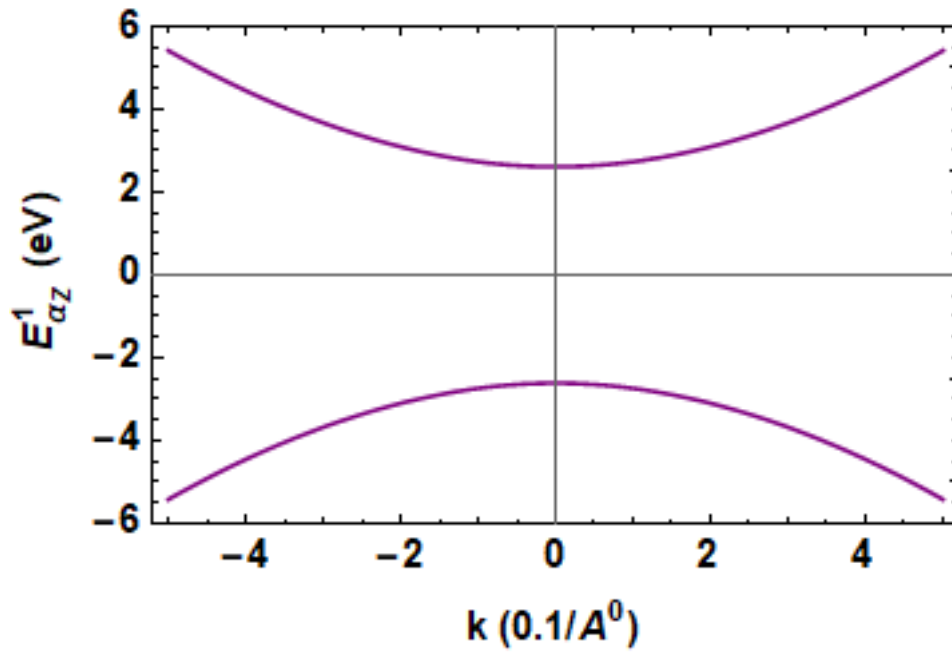


Figure 6(a): 2D plot of the photo-induced energy spectrum $\pm E_{\alpha_z}^{(1)}(k)$ for $\alpha_z = 1$

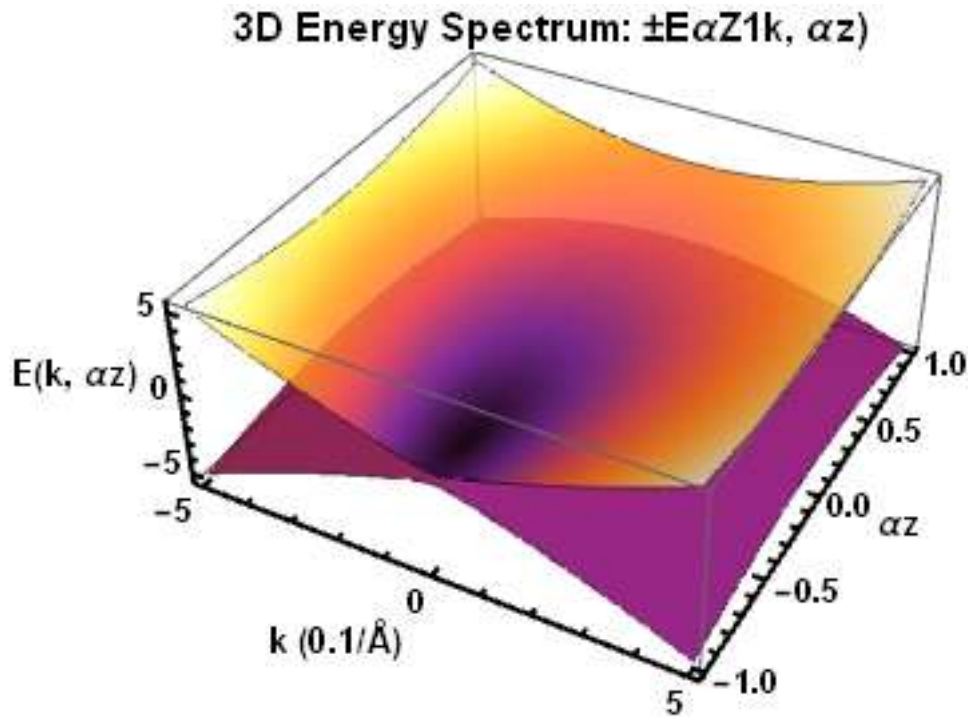


Figure 6(b): 3D surface plot showing dependence of energy spectrum on both k and α_z . The light-matter interaction modifies the band structure, creating energy gaps and curvature changes.

The application of circularly polarized off-resonant light modifies the original Dirac-like band structure through virtual photon absorption and emission. This modification is captured in the Floquet formalism by introducing renormalized terms in the Hamiltonian. The resulting energy bands, plotted in Fig. 6, show significant band gap enhancements and curvature deformations, both dependent on the light amplitude A_0 and frequency Ω .

These changes lead to new topological regimes, characterized by altered Chern numbers and Berry curvature behavior, as discussed in later sections. Notably, the appearance of a light-induced mass term $m_{\Omega} = \frac{(\hbar v_f A_0)^2}{\hbar \Omega}$ plays a vital role in controlling the gap size and hence the topological transition.

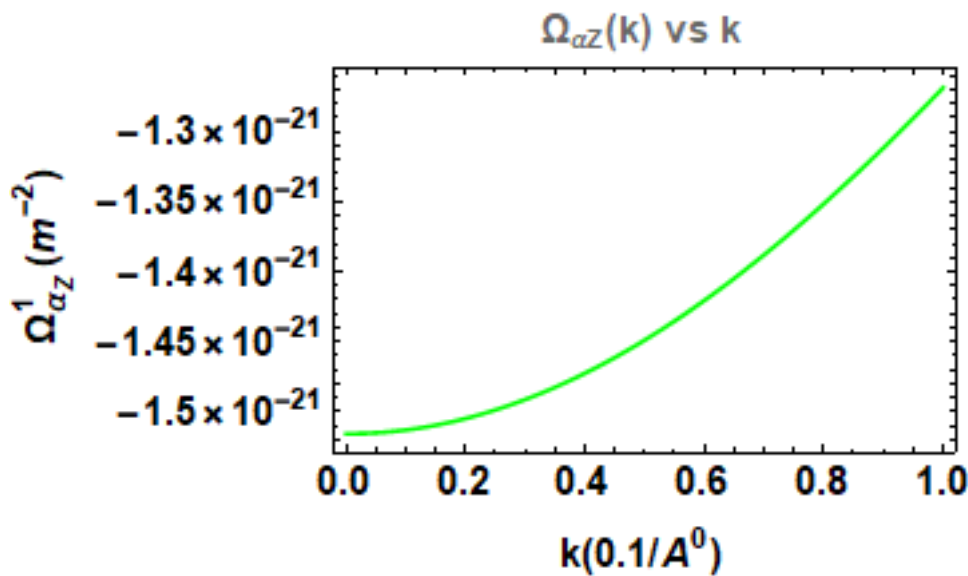


Figure 7(a): 2D Berry curvature $\Omega_{\alpha_z}(k)$ plot for light Hamiltonian with $\alpha_z = +1$

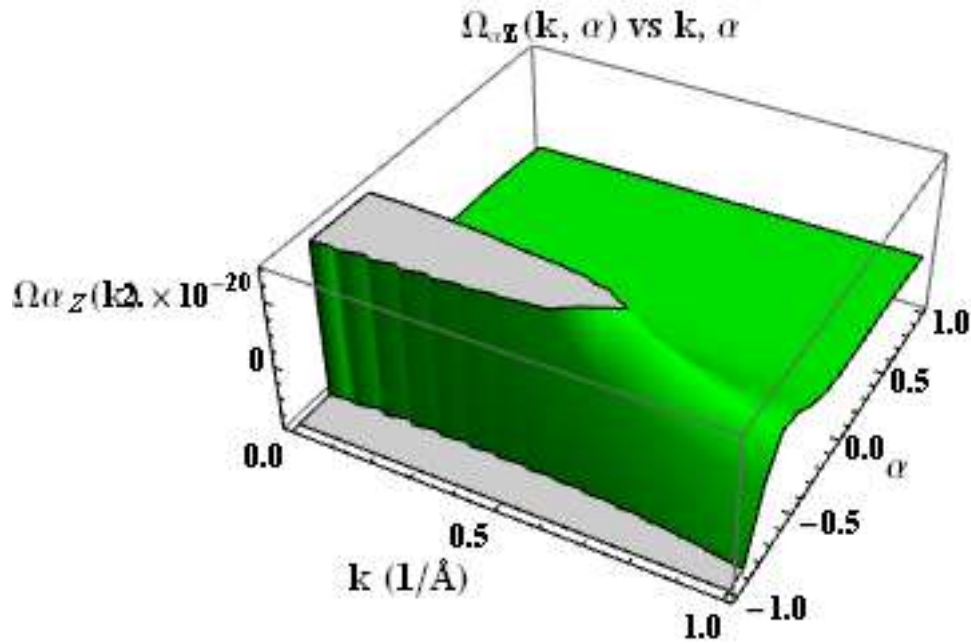


Figure 7(b): 3D Berry curvature $\Omega_{\alpha_z}(k)$ plot for light-induced Hamiltonian showing evolution with α_z .

The plots in Figure 7 illustrate the behavior of the Berry curvature $\Omega_{\alpha_z}(k)$ for the light-induced Hamiltonian. In the left plot (2D), the Berry curvature is shown as a function of k for fixed helicity $\alpha_z = +1$. The curvature reaches its maximum near $k = 0$ and gradually decreases with increasing k . This localized behavior near the origin indicates that the central region contributes dominantly to the topological characteristics of the system. In the right plot (3D), the Berry curvature is plotted as a function of both k and α_z . The surface shows symmetry with respect to α_z , highlighting how different light helicities affect the Berry curvature profile. The plot confirms that the topological response can be controlled by tuning the parameters of the driving field. These plots support the presence of light-induced topological phase transitions by revealing the modification of Berry curvature under external periodic driving.

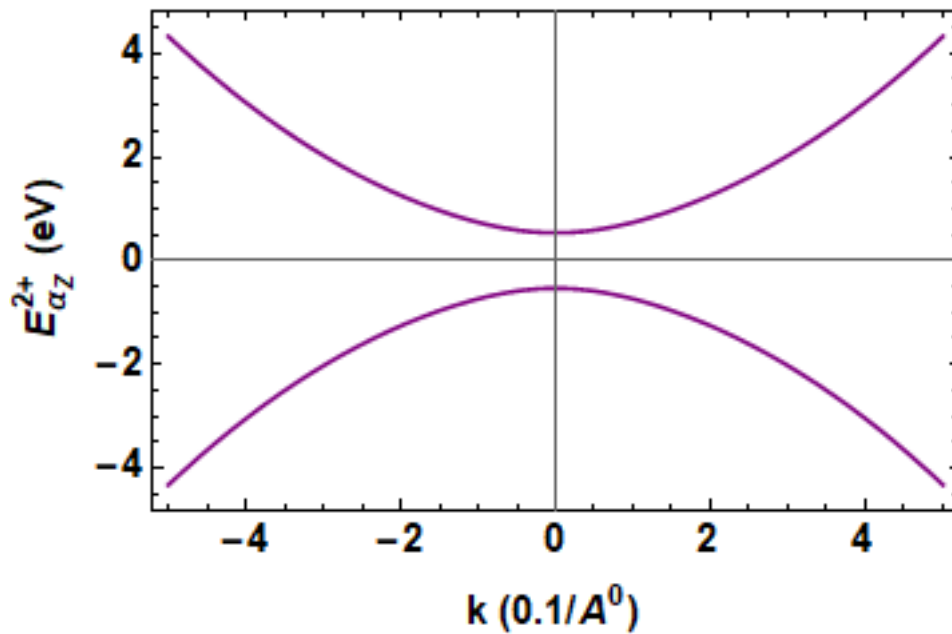


Figure 8(a): Energy dispersion $\pm E'_{\alpha_z}(k)$ for the light-induced Hamiltonian 2D plot of positive and negative energy bands for $\alpha_z = +1$.

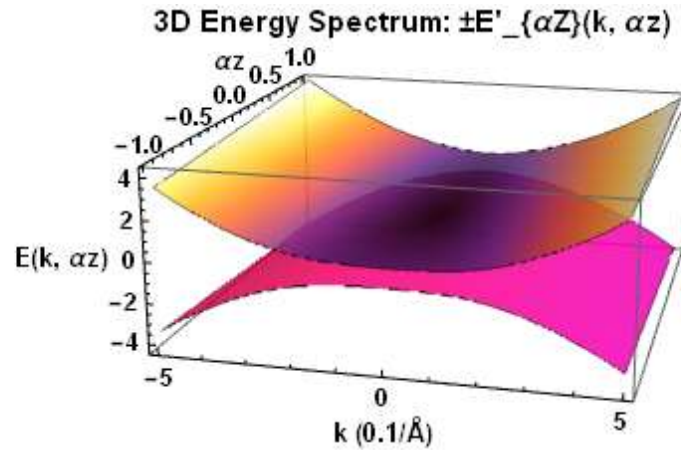


Figure 8(b): 3D energy spectrum showing variation with α_z .

Figure 8 displays the energy dispersion $\pm E'_{\alpha_z}(k)$ for the light-induced Hamiltonian that includes the quadratic kinetic energy term $\frac{\hbar^2 k^2}{2m'}$. The left plot shows the 2D energy bands for $\alpha_z = +1$. The spectrum exhibits a symmetric structure around $E = 0$, where the conduction and valence bands are separated by a momentum-dependent gap. The influence of the mass term m' and momentum k leads to a non-linear dispersion, especially for higher values of k . In the right 3D plot, the energy spectrum is extended over both k and α_z . This surface highlights how the band structure evolves with the helicity of light. The gap opening is more pronounced around $k = 0$, and the curvature changes gradually with α_z , which emphasizes the tunability of the band structure using circularly polarized light. These results confirm the modification of quasiparticle energies under periodic driving and support the presence of light-induced topological phenomena in the system.

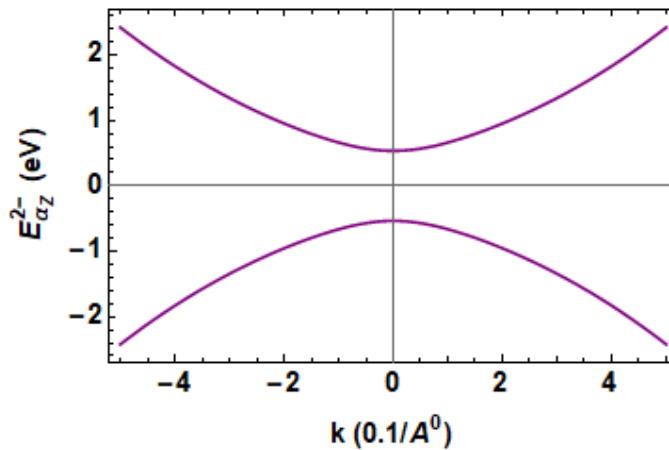


Figure 9(a): Energy dispersion $\pm E''_{\alpha_z}(k)$ with negative square root term in the Hamiltonian of 2D plot for $\alpha_z = +1$.

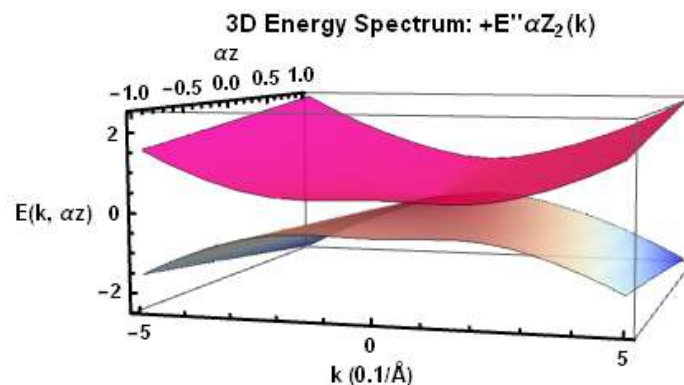


Figure 9(b): 3D spectrum showing variation with α_z .

Figure 9 illustrates the modified energy dispersion $\pm E''_{\alpha_z}(k)$ for the light-induced Hamiltonian with a negative square root term. In the left panel, the 2D energy spectrum is plotted for $\alpha_z = +1$, highlighting a distinct difference in band structure due to the sign reversal in the square root term. The presence of the kinetic energy term $\frac{\hbar^2 k^2}{2m'}$ still causes the dispersion to grow quadratically with momentum, but the subtraction of the square root component introduces a unique curvature, especially near $k = 0$. The right panel shows a 3D visualization of the energy bands as a function of both k and α_z . The

surface shows a dip around the origin and becomes flatter for higher k , indicating a reversal in energy curvature compared to the conventional form. This type of dispersion may be useful in modeling inverted band structures or special Floquet-engineered states. Such modifications in energy structure are significant in topological phase studies where tuning energy curvature can alter the Chern number and the nature of the edge states.

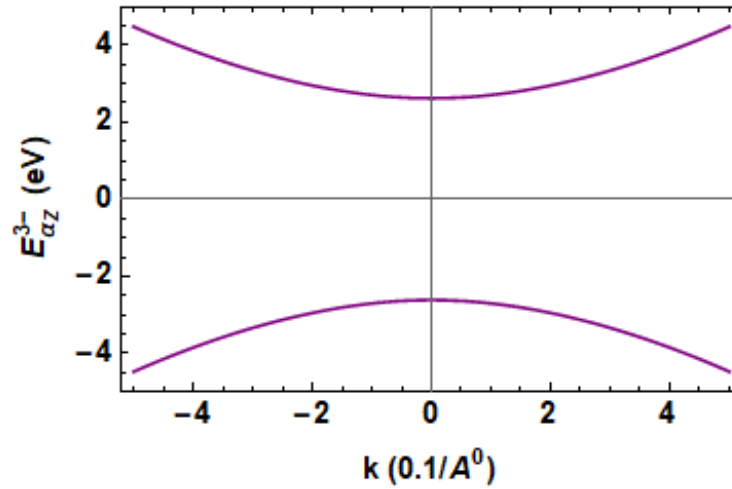


Figure 10(a): Photo-induced energy dispersion $\pm E''_{\alpha_z}(k)$ for the driven Hamiltonian under off-resonant light. Left: 2D plot for $\alpha_z = +1$.

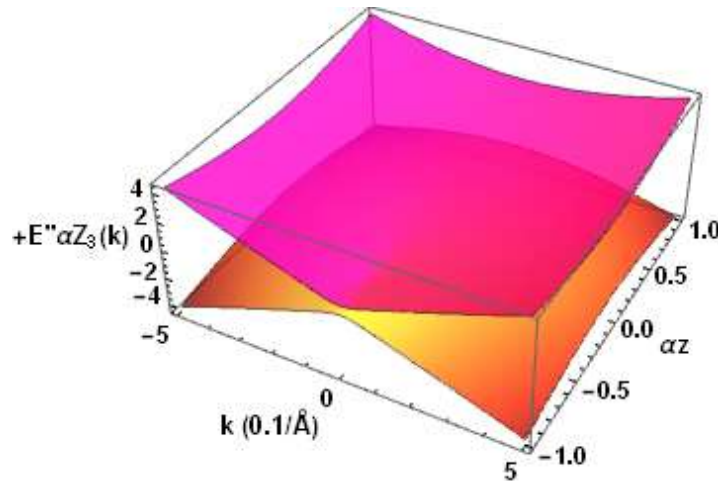


Figure 10(b): 3D Photo-induced energy dispersion $\pm E''_{\alpha_z}(k)$ for the driven Hamiltonian spectrum showing variation with α_z .

Figure 10 displays the energy spectrum $\pm E''_{\alpha_z}(k)$ for the photo-induced (light-dressed) Hamiltonian, where off-resonant circularly polarized light modifies the system parameters. The left panel shows the 2D band dispersion at $\alpha_z = +1$. The energy expression includes a renormalized velocity term η_{α_z} and an effective mass term m_{Ω} , both of which arise due to light-matter interaction. This results in a modified gap and curvature in the energy bands compared to the undriven case. The 3D plot (right) illustrates the full energy dispersion as a function of momentum k and spin polarization α_z . The asymmetry with respect to α_z becomes visible in both magnitude and shape of the energy bands, reflecting the role of light in breaking time-reversal symmetry. These results are crucial for identifying and controlling topological phase transitions via external light, as the gap size and dispersion curvature can directly affect Berry curvature and the resulting Chern number.

5 Discussion

The analysis presented in this work shows how the band structure and topological properties of magnetically doped topological insulator thin films are altered under circularly polarized off-resonant light. For the dark (undriven) Hamiltonian, the energy dispersion exhibits a symmetric Dirac-type band structure due to the quadratic momentum term. The addition of a magnetic exchange field opens a finite band gap, as confirmed by the numerical energy plots.

When the system is subjected to circularly polarized light, the Hamiltonian is modified through the Floquet formalism. This light-matter interaction renormalizes the Fermi velocity and introduces an additional mass term m_{Ω} , significantly altering the energy bands. The resulting asymmetry in the dispersion reflects the breaking of time-reversal symmetry, a key characteristic for observing photo-induced topological transitions.

Berry curvature plots for both the dark and light-driven systems highlight the central role of low momentum regions ($k \approx 0$) in determining the topological features. The curvature's dependence on α_z and the helicity of light indicates that the topological response can be finely tuned by adjusting external field

parameters. Furthermore, the calculated Chern numbers match the observed curvature behaviors and confirm the transition between distinct topological phases.

5 Conclusion

This study demonstrates that light can be used as an effective external tool to engineer and control topological phases in Dirac materials. By including the quadratic momentum term in the Hamiltonian and using Floquet theory to account for periodic driving, we show the transition from Quantum Anomalous Hall Insulator (QAHI) to Quantum Pseudo-Spin Hall Insulator (QPHI) phases under varying light parameters.

Our energy and Berry curvature analyses confirm that both the band structure and topological invariants are strongly influenced by circularly polarized light. These findings provide theoretical support for experimental realization of light-induced topological phase transitions and open new pathways for designing tunable quantum materials for spintronics and optoelectronic devices.

6. Acknowledgement

I express my deepest gratitude to my supervisor, Madam Kulsoom Rahim, for her great guidance and support during this research. Special thanks go to UET Taxila and its Department of Basic sciences for providing resources. I also appreciate my colleagues and peers for discussing them with insightful discussions and encouragement. Last but not least, I want to thank my family for their unending support and patience.

7. References

- [1] M. Z. Hasan and C. L. Kane, "Topological insulators," *Reviews of Modern Physics*, vol. 82, no. 4, pp. 3045–3067, 2010.
- [2] X.-L. Qi and S.-C. Zhang, "Topological insulators and superconductors," *Reviews of Modern Physics*, vol. 83, no. 4, pp. 1057–1110, 2011.
- [3] C.-Z. Chang et al., "Experimental observation of the quantum anomalous Hall effect in a magnetic topological insulator," *Science*, vol. 340, no. 6129, pp. 167–170, 2013.
- [4] R. Yu et al., "Quantized anomalous Hall effect in magnetic topological insulators," *Science*, vol. 329, no. 5987, pp. 61–64, 2010.
- [5] T. Oka and H. Aoki, "Photovoltaic Hall effect in graphene," *Physical Review B*, vol. 79, no. 8, p. 081406, 2009.
- [6] N. H. Lindner, G. Refael, and V. Galitski, "Floquet topological insulator in semiconductor quantum wells," *Nature Physics*, vol. 7, no. 6, pp. 490–495, 2011.
- [7] Y. Wang, H. Steinberg, P. Jarillo-Herrero, and N. Gedik, "Observation of Floquet-Bloch states on the surface of a topological insulator," *Science*, vol. 342, no. 6157, pp. 453–457, 2013.
- [8] B. A. Bernevig, T. L. Hughes, and S.-C. Zhang, "Quantum spin Hall effect and topological phase transition in HgTe quantum wells," *Science*, vol. 314, no. 5806, pp. 1757–1761, 2006.
- [9] F. D. M. Haldane, "Model for a quantum Hall effect without Landau levels: Condensed-matter realization of the 'parity anomaly'," *Physical Review Letters*, vol. 61, no. 18, pp. 2015–2018, 1988.
- [10] P. Hosur and X. Qi, "Recent developments in transport phenomena in Weyl semimetals," *Compte Rendus Physique*, vol. 14, no. 9–10, pp. 857–870, 2013.
- [11] G. B. Halász and L. Balents, "Time-reversal invariant realization of the Weyl semimetal phase," *Physical Review B*, vol. 85, no. 3, p. 035103, 2012.
- [12] J. Shao and G. Yang, "Magneto-optical conductivity of Weyl semimetals with quadratic term momentum," *AIP Advances*, vol. 6, no. 2, p. 025312, 2016.
- [13] P. E. Ashby and J. Carbotte, "Magneto-optical conductivity of Weyl semimetals," *Physical Review B*, vol. 87, no. 24, p. 245131, 2013.
- [14] W. Y. Shan, H. Z. Lu, S. Q. Shen, *New J. Phys.* **12**, 043048, 2010.
- [15] Y. Zhang, K. He, C. Z. Chang, C. L. Song, L. L. Wang, X. Chen, J. F. Jia, Z. Fang, X. Dai, W. Y. Shan, S. Q. Shen, *Nat. Phys.* **6**, 584, 2010.
- [16] C. X. Liu, H. J. Zhang, B. Yan, X. L. Qi, T. Frauenheim, X. Dai, Z. Fang, S. C. Zhang, *Phys. Rev. B* **81**, 041307(R), 2010.
- [17] V. Kulbachinskii, P. M. Tarasov, and E. Brük, *JETP Lett.* **73**, 352 (2001).
- [18] H. Zhang, C.-X. Liu, X.-L. Qi, X. Dai, Z. Fang, S.-C. Zhang, *Nat. Phys.* **5**, 438, 2009.
- [19] T. Kitagawa, E. Berg, M. Rudner, E. Demler, *Phys. Rev. B* **82**, 235114, 2010.
- [20] M. Ezawa, *Phys. Rev. Lett.* **110**, 2, 026603, 2013
- [21] M. Bukov, L. D'Alessio, A. Polkovnikov, *Advances in Physics*, **64**, 2, 139–226, 2015.

-
- [22] E. Prodan, Phys. Rev. B **80**, 125327 (2009).
- [23] D. N. Sheng, Z. Y. Weng, L. Sheng, and F. D. M. Haldane, Phys. Rev. Lett. **97**, 036808 (2006).
- [24] H. Li, L. Sheng, D. N. Sheng, D. Y. Xing, Phys. Rev. B **82**, 165104 (2010).
- [25] S. Li, L. Hui-Chao, Y. Yun-You, S. Dong-Ning, X. Ding-Yu, Chinese Phys. B **22**, 067201 (2013).
- [26] C. L. Kane and E. J. Mele, Phys. Rev. Lett. **95**, 146802 (2005).